FULL PAPER

# Molecular and Genomic Impact of Large and Small Lateral Dimension Graphene Oxide Sheets on Human Immune Cells from Healthy Donors

*Marco Orecchioni, Dhifaf A. Jasim, Mario Pescatori, Roberto Manetti, Claudio Fozza, Francesco Sgarrella, Davide Bedognetti, Alberto Bianco, Kostas Kostarelos,* and Lucia Gemma Delogu**

**Graphene oxide (GO) is attracting great interest in biomedical sciences. The impact of GO on immune cells is one fundamental area of study that is often overlooked, but critical in terms of clinical translation. This work investigates the effects of two types of thoroughly characterized GO sheets, different in their lateral dimension, on human peripheral immune cells provided from healthy donors using a wide range of assays. After evaluation of cell viability, the gene expression was analyzed, following GO exposure on 84 genes related to innate and adaptive immune responses. Exposure to GO small sheets was found to have a more significant impact on immune cells compared to GO large sheets, reflected in the upregulation of critical genes implicated in immune responses and the release of cytokines IL1$\beta$ and TNF$\alpha$. These findings were further confirmed by whole-genome microarray analysis of the impact of small GO sheets on T cells and monocytes. Activation in both cell types was underlined by the overexpression of genes such as CXCL10 and receptor CXCR3. Significant energy-dependent pathway modulation was identified. These findings can potentially pave the foundations for further design of graphene that can be used for immune modulation applications, for example in cancer immunotherapy.**

## 1. Introduction

In the last few years, thanks to their remarkable characteristics and unique properties, there has been enormous interest in new nanomaterials (including graphene) among the scientific community and the public.[1,2] Pristine graphene and graphene oxide (GO) have been used in a growing number of biomedical applications for therapy and diagnosis such as drug delivery and photodynamic therapy.[1,3,4] Most studies have focused on GO,[5] due to its ability to be well-dispersed in aqueous media,[6] but more systematic studies are needed urgently to fully explore graphene in medicine.[7] To date the majority of reports have indicated accumulation of graphene-based materials (GBMs) in organs of the reticuloendothelial system, mainly liver, spleen, and lungs.[8,9] Immune cells are the initial

M. Orecchioni, Dr. M. Pescatori, Prof. F. Sgarrella, Dr. L. G. Delogu
Department of Chemistry and Pharmacy
University of Sassari
07100 Sassari, Italy
E-mail: lgdelogu@uniss.it
D. A. Jasim, Prof. K. Kostarelos
Nanomedicine Lab
Faculty of Medical and Human Sciences
The University of Manchester
Manchester M13 9PT, UK
E-mail: kostas.kostarelos@manchester.ac.uk
Dr. M. Pescatori
Heath-E-Solutions
Rotterdam, 3016 DL, The Netherlands
Prof. R. Manetti
Department of Clinical Medicine
and Experimental Oncology
University of Sassari
07100 Sassari, Italy
Dr. C. Fozza
Department of Biomedical Science
University of Sassari
07100 Sassari, Italy
Dr. D. Bedognetti
Research Branch
Sidra Medical and Research Centre
Doha, Qatar
Prof. A. Bianco
CNRS
Institut de Biologie Moléculaire et
Cellulaire, Laboratorie d'Immunopathologie et Chimie
Thérapeutique
67000 Strasbourg, France

DOI: 10.1002/adhm.201500606

biological components that interact with the GBM.[10] A recent study on GO in vivo biocompatibility indicated an inflammatory response typical of a foreign body reaction.[11] Wang et al., studied the toxicity of GO after injection in mice and found that GO at low (0.1 mg) and middle dose (0.25 mg) did not exhibit clear toxic effects, while at high dose (0.4 mg) the authors evidenced chronic toxicity. In addition the Authors underlined the importance of further work on the possible mechanism of interaction between GO and immune cells in human body or mice.[9]

Therefore, immunotoxicological evaluation is critical for future clinical developments of GBMs. The interactions and potential modulation of the immune system by GBM exposure may also offer interesting possibilities for immunotherapeutics or novel vaccination strategies.[12,13] The impact exerted by GBM is still unclear. Different studies reported good biocompatibility and no cellular damage after exposure to GBM,[14,15] while others have evidenced cell toxicity, manifested as enhanced apoptosis and necrosis.[16,17] Such discrepancies can be due to differences in the characteristics of GBM in terms of dimensions, functionalization and purity.

The impact of well-characterized GO of different dimensions on human monocyte-derived macrophages (hMDM) has been reported.[18] However, in order to offer further understanding of the differential impact between large and small graphene flakes on the immune system, cell populations, other than macrophages, present in the systemic blood compartment need to be intensively investigated. Sasidharan et al. have considered the immune cell functionality besides biocompatibility, focusing on a few classic response parameters such as activation markers and cytokine production.[19] Although these approaches can elucidate the effect of GO flakes on the expression of some specific proteins, they are limited in their ability to provide a reliable insight into a global genomic effect that better reflects overall impact of GO on the immune system. Our group previously described the effect of functionalized carbon nanotubes (f-CNTs) on immune cell activation.[20,21]

Moreover, we and others underlined the importance of looking at the genomic level by using large genome expression analysis and high-throughput technologies to better understand the overall impact into immune cells.[22,23] Recently, Chatterjee et al. used microarray analysis to investigate the effects on human liver cells of GO and reduced GO,[24] but, to our knowledge, no report has used large genomic data approaches to investigate the impact of GO materials on immune cells.

In this work, we employed two types of thin GO flakes (between one and two graphene layers) thoroughly characterized by transmission electron microscopy (TEM), atomic force microscopy (AFM), Raman spectroscopy, and several other techniques to determine lateral dimensions, number of graphene layers, and surface properties. Human peripheral blood mononuclear cells (PBMCs) from healthy donors were used. This pool of immune cell populations was able to provide closer relevance and insight to clinical conditions, better than cell lines or specific subpopulations. The extent of early and late apoptosis, necrosis, cell activation, and cytokine release were determined following exposure to the GO materials. The impact on 84 genes related to the immune response was then analyzed. Finally, whole genome analysis was conducted on T lymphocytes (Jurkat cells) and monocytes (THP1 cells) as representative populations of the adaptive and innate immune responses.

## 2. Results

### 2.1. GO Material Characteristics

Structural characterization using TEM and AFM imaging techniques of small GO sheets (GO-S) and large GO (GO-L) is shown in **Figure 1**A and Figure S1A–D (Supporting Information). The lateral size distribution is shown in Figure 1B for GO-S (<1μm), and GO-L (1–10 μm) determined from analysis of several TEM images. AFM height images revealed that the sheets were one or two layers thick (1–2 nm). Thickness distribution for GO-S is shown in Figure S1E (Supporting Information); However, for GO-L it was technically more challenging to obtain accurate thickness distributions due to folding and wrinkling that commonly measurements. Despite that, in the few GO-L sheets accurately measured, thickness between 1 and 2 nm was observed. Fourier transform infrared spectroscopy (FT-IR) was used to identify the functional groups on the surface of GO (Figure 1C). Both GO samples showed a broadband ≈3100–3600 $cm^{-1}$ due to the O—H stretching vibrations, and an intense peak at 1730 $cm^{-1}$ for the C=O stretching vibrations. Aromatic and unsaturated bonds were apparent by the intense band at 1590 $cm^{-1}$. Several bands were detected ≈1000-1250 $cm^{-1}$ for the C—O and C—O—C stretching vibrations.[25] FT-IR spectra confirmed that the oxidation resulted in the formation of hydroxyl, carboxyl, and oxide groups with the presence of aromatic regions, typical of GO materials,[26] with very little differences between the two types of GO (the starting graphite material did not show any distinct peaks in the FT-IR spectrum).

Quantification of the functional groups was also assessed by thermogravimetry (TGA) (Figure 1D). TGA curves for the two GO materials and the starting graphite were obtained. Two main weight loss steps were observed after subtracting 10% due to evaporation of the water content up to 100 °C (Table S1, Supporting Information). The first mass loss in the TGA curves between 100 and 260 °C was due to the decomposition of the labile oxygen groups (such as carboxylic and aldehyde groups) and the removal of any residual water. The second weight loss occurred between 260 and 460 °C and was due to the pyrolysis of the stable oxygen groups (mainly epoxides).[27] No significant differences in the TGA melting curves were detected between GO-S and GO-L material. However, they were both significantly higher than graphite, which further confirmed their extensive surface oxidation. Raman spectra (Figure 1E) indicated bond stretching of $sp^2$ hybridized carbon atoms resulted in the distinct Raman G band ≈1590 $cm^{-1}$[28] in all samples. This band appeared wider and slightly blueshifted in both GO samples compared to graphite. The D band at 1330 $cm^{-1}$ due to disorder[29] created during oxidation was more distinct in the GO samples, while the 2D band near 2700 $cm^{-1}$ disappeared, compared to the starting graphite. The D-to-G band intensity ratio ($I_D/I_G$), corresponding to a disorder metric[28] is

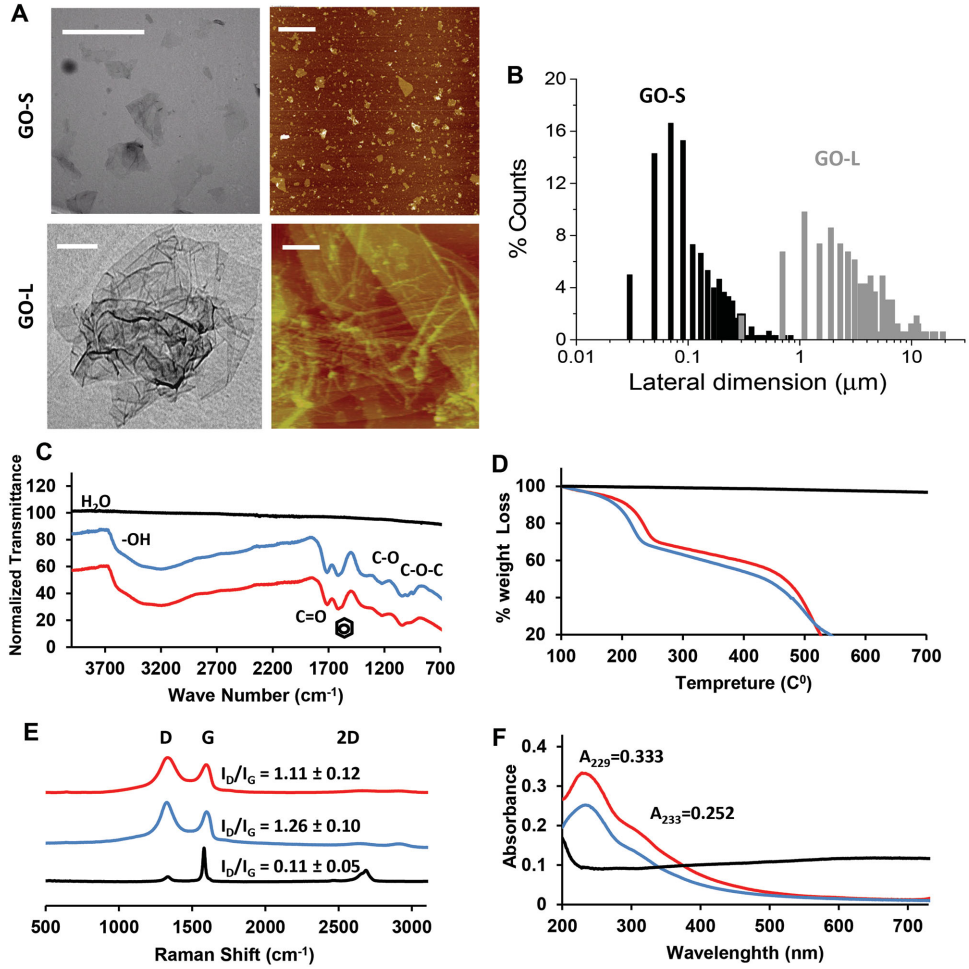


**Figure 1.** Physicochemical characterization of GO-S and GO-L. A) Representative TEM images (left) and AFM images (right) of GO-S and GO-L (all scale bars are 1.5 μm); B) Size distribution detected by counting more than 100 GO sheets from several TEM images of GO-S and GO-L; C–F) FT-IR spectra, TGA curves, Raman and UV–visible spectra, respectively, for GO-S (red curves) and GO-L (blue curves) compared to the started graphite (black curves).

also shown for each spectra (Figure 1E). No statistical significance (using *Student's t-test*) was detected between the two GO samples (GO-S and GO-L) in both $I_D/I_G$ ratio and also in the D band width; however, both were significantly different from the starting graphite.

In terms of surface charge, both GO samples were strongly negative, due to the multiple surface oxygen groups (Figure S1F, Supporting Information), but GO-L was of slightly higher negativity compared to GO-S. UV–vis spectroscopy was then used to confirm the optical properties of the GO structures. Both GO samples showed a characteristic absorbance peak ≈230 nm, with a shoulder ≈300 nm with slight difference between the two samples, while graphite had featureless spectrum with high scattering due to the poor aqueous solubility (Figure 1F). Such absorbance peaks have been described to arise from the delocalization of the $\pi$ electrons due to the oxidation process, the 230 nm peak due to C—C transitions, while that at 300 nm due to C=O transitions.[30]

### 2.2. Cell Viability and Activation Markers

The first step in the interaction with immune cells was to study the impact in dose response of the two GO materials on cellular viability of PBMCs from healthy donors (**Figure 2**). Different stainings for flow cytometry analysis were performed to detect: (i) early apoptosis, (ii) late apoptosis, and (iii) necrosis. Annexin V staining showed the absence of a significant number of early apoptotic cells in treated samples at all tested GO concentrations (Figure 2A). An amine-reactive fluorescent staining was used to detect cells with compromised membranes (late apoptotic and necrotic cells) (Figure 2B). The materials did not show significant cell toxicity. The only exception was a reduction in cell viability at high doses (75 μg $mL^{-1}$) for GO-S. The percentage of dead cells was then evaluated by propidium iodide staining (Figure 2C). Cell viability at exposures of 25 μg $mL^{-1}$ GO was similar to controls, whereas at GO concentrations of 50 and 75 μg $mL^{-1}$ PBMCs displayed

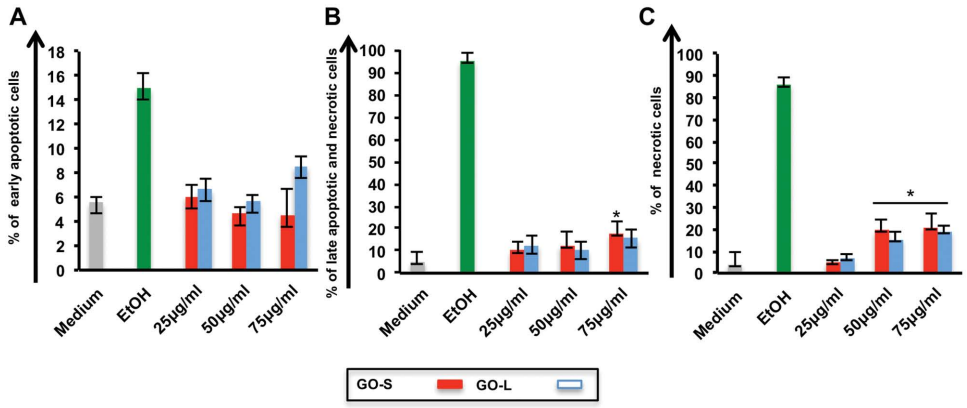


**Figure 2.** Viability of human primary immune cells. PBMCs were incubated for 24 h with GO-S and GO-L at increasing doses of 25, 50, and 75 μg $mL^{-1}$ or left untreated (medium), ethanol was used a positive control. A) Early apoptosis was assessed by Annexin V staining. B) Data from staining with an amine-fluorescent dye able react with amine free of compromised membranes of late apoptotic and necrotic cells. C) Necrotic cells detected with propidium iodide staining. Experiments were carried out at least in triplicate and analyzed by flow cytometry (*$P$-value < 0.05).

mortality levels ranging between 15% and 20%, a statistically significant value when compared to the controls, but still very low in relation to the positive controls (Figure 2). To investigate the functional impact of GO exposure on primary immune cells, considering their activation as a crucial endpoint, we measured the expression of CD69 and CD25 markers (Figure S2, Supporting Information). CD69, a member of the C-type lectin superfamily (Leu-23), is one of the earliest cell surface antigens expressed by immune cells following activation, while CD25 (alpha chain of the IL-2 receptor) is a late activation antigen. CD69 and CD25 expression in GO-exposed samples was comparable to the untreated negative controls (Figure S2, Supporting Information).

### 2.3. Immune Gene Expression Array

To evaluate the possible effect on key pathways controlling innate and adaptive immune response, we performed a deep genomic analysis on the expression of a large number of highly selected immune genes (**Figure 3**). The impact on GO-L or GO-S treated PBMCs was assessed by an 84 immune genes array. As a first step, the expression ratio between GO-L or GO-S and control samples for all 84 genes were clustered and displayed as heat map where individual elements of the plot are colored according to their standardized expression values (Figure 3A; red squares: upregulated genes; green squares: downregulated genes). The major impact on gene expression due to GO-S exposure was apparent when compared to the values obtained for GO-L (heat map values and gene names are reported in Figure S3, Supporting Information). To better illustrate the different effects between GOs on the gene expression, the standardized expression values of modulated genes are also displayed as a heat-map detail in the Figure 3B for the control, GO-S and GO-L samples, respectively (Figure 3B; red squares: high expression; green squares: low expression). The bright red strip marks indicate the enhanced effects of GO-S compared to GO-L. All genes reported in Figure 3B were upregulated in GO-S, while GO-L samples displayed values similar to the untreated controls. By using a fold regulation cutoff (FR > 4, both directions) we identified 16 upregulated genes for GO-S and five upregulated genes for GO-L (Figure 3C,D).

Moreover, we found that GO-L was able to induce downregulation of four immune genes compared to only one of GO-S with a fold change less than 4 (Figure 3C,D). Most modulated genes were upregulated compared to control samples, as it can also be more easily observed in the scatter plot shown in Figure 3C. Some of the genes that offered a statistically significant difference in expression were: CSF2, TNF, IL6, IL10, CD80, IL1, IL1R1, TICAM1, IL8, IL23A, NFKB1, TBX21, CD40, CCR6, and IFNAR1. All of them were upregulated at least fourfold in GO-S treated samples. A list of all modulated genes by GO-S and GO-L exposure, in terms of at least a fourfold down or upregulated, is displayed in Figure 3D. To better understand the involvement of specific pathways in the possible immune system modulation process triggered by GOs, we looked at the expression of specific groups of genes involved in controlling precise signaling aspects of the immune response (Figure 3E). By looking at the RNA expression levels as $2^{-\text{avg }\Delta Ct}$ values, we queried several pathways including Th1 and Th2 immune response, pattern recognition receptor (in particular toll-like receptors), cytokines/chemokines, and cytokine receptors. We observed that following GO-S treatment, a marked upregulation of genes involved in the Th1 immune response such as CD80 and TBX21 occurred (Figure 3E). Regarding the toll-like receptor (TRL) pathways, TLR3, TLR5, and TLR9 showed a fold regulation greater than 2 (Figure S4, Supporting Information). The most regulated was TLR2 by GO-S ($p$-value < 0.05) (Figure 3E). Cytokines/chemokines and cytokine receptors upregulated by GO-S ($p$-value < 0.05) were: IL1R1, IFNAR1, CSF2, TNF, CCL5, IL6, IL1$\alpha$, IL1$\beta$, and IL8.

### 2.4. Cytokine Secretion Assay

To investigate the cytokine production, multiplex Enzyme-Linked Immunosorbent Assay (ELISA) was used to measure

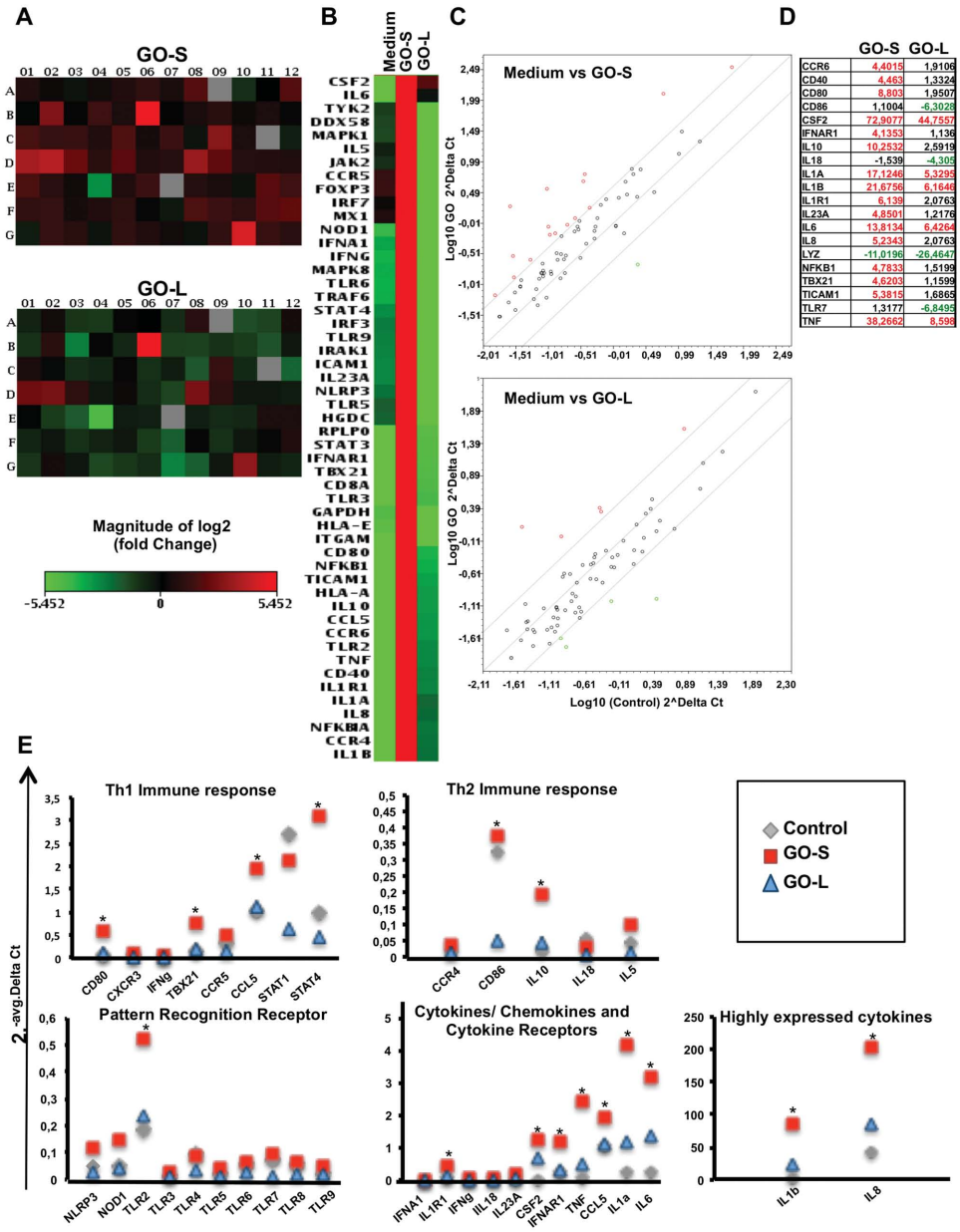


**Figure 3.** Immune gene expression array. A) Heat-map comparison of 84 genes after exposure to GO-S or GO-L. Genes were displayed for fold-change variations in respect to the controls and colored by their standardized expression value (red: high expression; green: low expression). B) Heat-map detail showing the immune transcript upregulated by GO-S in PBMCs; data are reported as mean of experiments carried out in triplicate. C) Scatter plots chart. Genes upregulated with fold change greater than 4 are showed with red round; gene with fold change less than 4 are showed with green round; in black unmodulated genes. D) Table of modulate genes in GO-S and GO-L versus control. Red shows genes with a fold change greater than 4, green shows genes with a fold regulation less than 4. E) Analysis of representative GO-S and GO-L modulated genes, summarized into their own pathways expressed as 2 Δct values (*$P$-value < 0.05).

IL1$\beta$, TNF$\alpha$, IL10, IL6, IL8, IL2, IFN$\gamma$, IL4, and CCL5 (**Figure 4**). Both types of GO are able to stimulate the release of some of the cytokines analyzed such as IL1$\beta$, IL1$\alpha$, TNF$\alpha$, and IL10 ($p$-value < 0.05). The production of IL1$\beta$, TNF$\alpha$, and IL10 was significantly induced by GO-S exposure (Figure 4A). IL6 and IL8 increased equally following treatment with either types of GO (Figure 4B). On the other hand, IL2, IFN$\gamma$, IL4, and CCL5 production was not stimulated by either GOs (Figure 4C).

### 2.5. Whole Genome Expression Analysis

Since a significant impact from GO-S exposure was revealed in terms of immune-related gene and protein upregulation, we wanted to further investigate the effects on whole-genome expression at a higher definition. To achieve this goal we used the microarray approach (Illumina Beadchip technology) looking at more than 47 000 genes on GO-S treated T lymphocyte cell line (Jurkat cells) and monocyte cell line (THP1 cells).

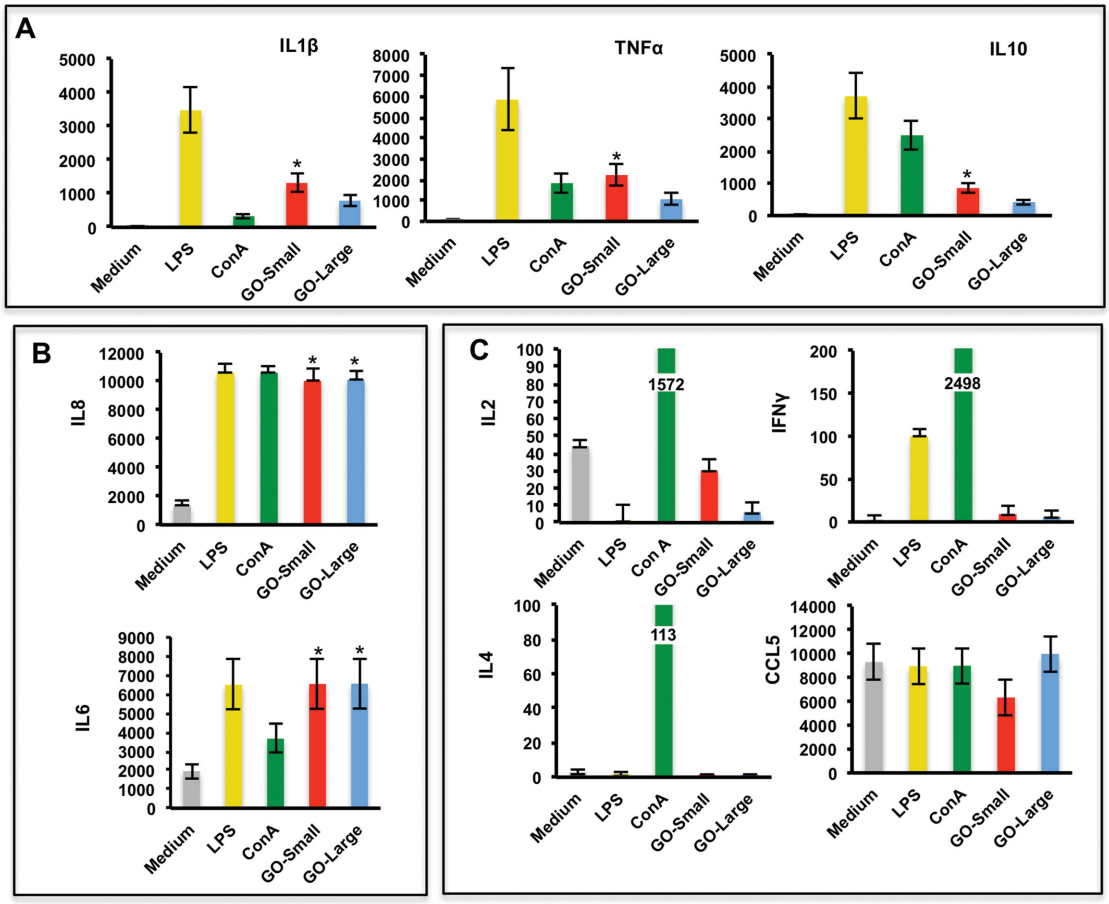


**Figure 4.** Cytokine secretion assay. Cytokine release was assessed by ELISA on PBMCs. Cells were incubated with GO-S and GO-L at 50 μg mL$^{-1}$. After 24 h the supernatants were collected and analyzed for the secretion (expressed in pg mL$^{-1}$) of the following cytokines and chemokines: A) IL$\beta$, TNF$\alpha$, IL10; B) IL8, IL6; C) IL2, IL4, IFN$\gamma$, CCL5.

Unsupervised multidimensional scaling evidenced four well-separated clusters identifying the cell type and the GO-S treatment as the parameters correlated to the first two components of variability (**Figure 5**A). To compute the probability of genes being differentially expressed, we used a random variance *t*-test as implemented in BRB-ArrayTools. To control the false discovery rate (FDR) in our list of genes, we used a permutation test to provide evidence that familywise error rate was less than 5% within the 80% confidence interval (CI). Using this cutoff values, we identified, for T cells, 738 genes upregulated (Fold Change (FC) > 1) and 409 genes downregulated (FC < 1) out of 1147 genes differentially expressed (Table S2, Supporting Information). In monocytes, 243 genes were upregulated (FC > 1) and 333 were downregulated (FC < 1) out of 576 total genes identified, compared to the control group (Table S3, Supporting Information).

As it can be observed in Tables S2 and S3 (Supporting Information) all genes passing the cut-off value were tabulated along with parametric *p*-value, fold change and links to major annotation sources. We clustered in a Venn diagram the genes differentially expressed in three groups (T cells, both T cells and monocytes, and monocytes) and displayed their standardized expression values as heat maps (Figure 5B). Only 341 significantly modulated genes were common in both cell lines, and only one of these was differently regulated. We searched for evidence suggesting the consistency of our gene expression data with known features of the analyzed cell lines and with the results from our previous experiments in the immune gene arrays (Figure 3).

The previous observations made using the immune array were confirmed since the analysis showed increased expression of genes such as: IL10, CCL5, CCR6, TYK2, IFNAR1, IRAK1, STAT6 in both cell types, CSF2, HLA-A, IL18, TLR9, and NFKB1 in T cells and DDX58, TLR3, TLR6, TLR7, and STAT3 in monocytes. To better understand at the mechanistic level, the physiological significance of the changes in gene expression, we used the gene set comparison tool in BRB-ArrayTools to assign the functional category definitions according to the Gene Ontology Database. As a result, 559 and 532 gene sets were scored as significantly modulated in monocytes and T cells, respectively (Tables S4 and S5, Supporting Information).

The immune activation mediated by GO-S was confirmed by the over expression of some relevant pathways: T cell migration, regulation of T cell chemotaxis, macrophage activation, receptor signaling involved in phagocytosis, and

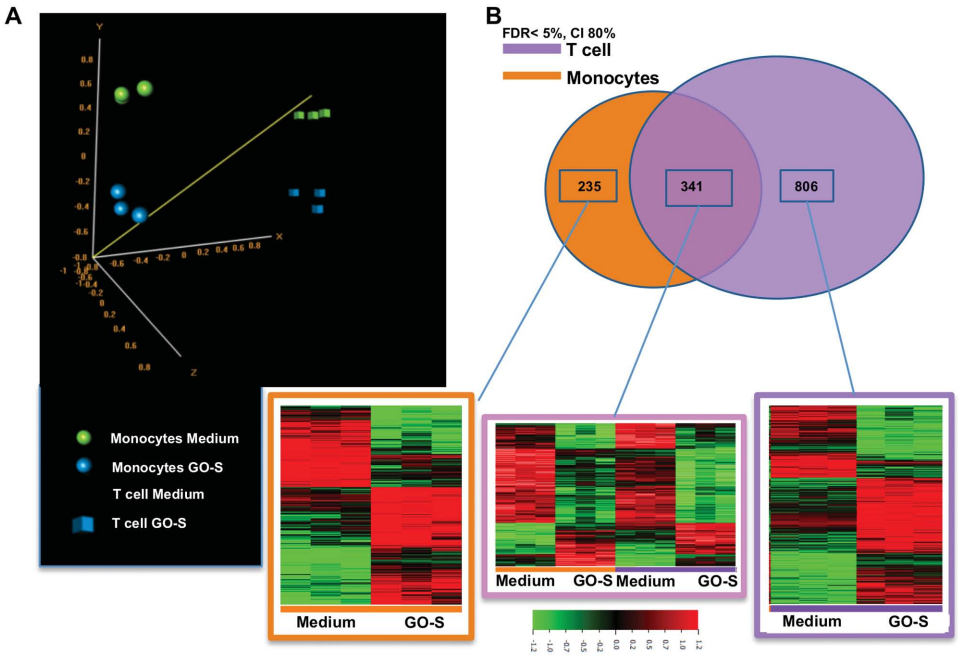


**Figure 5.** Gene expression analysis. A) 3D cluster graph identifies two different cell types treated and untreated with 50 μg $mL^{-1}$ of GO-S. B) Heat map and Venn diagrams show the number of probe sets differently modulated by comparison of T cell and monocytes gene sets resulting after GO-S treatment. Overlapping area indicate the number of transcripts commonly modulated in both cell types. The heat map indicates the change in expression in each subset (red: high expression; green: low expression).

leukocyte chemotaxis pathways (**Figure 6**A). In particular, we found an upregulation of genes closely related to inflammation such as CCL5 and the induction of chemokine genes such as CXCL10 and receptor CXCR3 (Figure 6A, red box). We confirmed the data using the ingenuity pathways analysis (IPA) software. Figure 6B highlights the upregulation of some genes that correlated with inflammation, illustrating the GO-S induced activation in T cells. On monocytes, the IPA analysis did not reveal a significant activation on the same pathway.

IPA shown also the induction of the IL10 expression pathway in T cells, by which we saw a clear upregulation of IL10 and IL10R genes (Figure S5A, Supporting Information). IL10 overexpression is IL1 mediated by the induction of SP1 transcription factor (Figure S5A, Supporting Information). By contrast the absence of stimulation of IFN$\gamma$ was confirmed with the IFN$\gamma$ pathway analysis. We have seen a marked downregulation of STAT1 in T cells, the principal effector of IFN$\gamma$ mediated cell activation (Figure S5B, Supporting Information).

Modification of cell metabolism was evident in both cell lines, characterized by the downregulation of transcripts involved in the oxidative phosphorylation (OX-PHOs), mitochondrial Adenosine TriPhosphate (ATP) synthesis coupled proton transport and protein synthesis (large and small ribosomal subunit pathways) (Figure S6, Supporting Information), including cellular and mitochondrial ribosomal S and L proteins such as: RPS17, RPS26, RPS27, RPS27A, RPL4-RPL10, and RPL39L (Figure S6, Supporting Information). Conversely, transcripts encoding glycolytic enzymes were upregulated (Figure S6, Supporting Information).

## 3. Discussion

There is a rapidly growing literature on the use GBMs particular in their oxide form (GO) for biomedical uses.[6,31] Compared to carbon nanotubes,[20,32] graphene has a larger available surface area[33] making it highly promising in the context of drug delivery and imaging.[34] As for any other nanomaterial designed to be a drug carrier, it is important to understand the possible adverse responses to GO and particularly its impact on the immune system.[35] Until today, there has been an inconclusive discussion whether GO should be considered immune compromising or not.[12] As we previously reported for CNTs, the immune impact could be different between GOs with different lateral dimensions and functionalization.[12] Sasidharan et al. underlined that the toxicity effects of pristine graphene toward macrophage cells can be easily averted by surface functionalization.[16,19] However, other studies are needed on the effect of different functionalized GOs on immune cells ex vivo and in vivo in order to assess the appropriate functionalization strategy.

The present study reports on the impact at the molecular level of well-characterized GOs on primary human immune populations. Previous works have studied only one or two cell population types, not in a complex human ex vivo cell pool.[19,36] We carried out the present study on PBMCs from healthy donors that included different cell populations, T cells, B cells, monocytes, dendritic cells, and natural killer cells to better reflect the effects on the pool of cell populations relevant to in vivo immune responses.

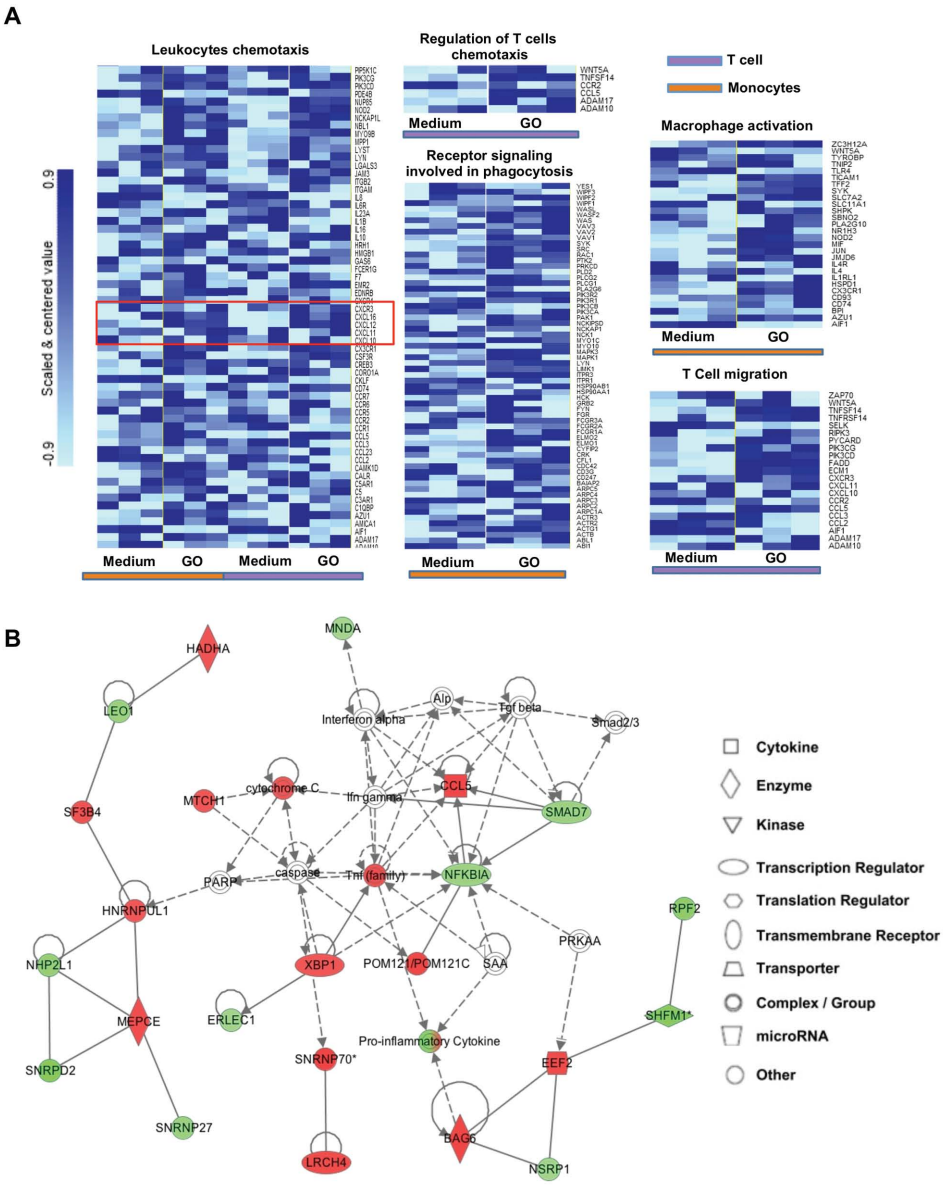


**Figure 6.** Gene expression of GO-S modulated pathways. A) Heat map representation of relevant modulated pathways using Gene Ontology categories. B) Inflammation pathway in T cells after treatment with GO-S. The image was done with Ingenuity software. Bold lines indicate direct interaction and dotted lines indicate indirect interaction. Genes upregulated by GO-S are highlighted in red and genes downregulated are highlighted in green.

Regarding the graphene material characteristics, the question of whether the GO lateral dimensions can be a determinant factor of biological effects has been highlighted.[4] In this study, GO of two different sizes (GO-S and GO-L) were prepared and characterized in terms of shape, structure, lateral size, thickness, oxygenated functional groups, optical, and surface properties. The two GO samples were only significantly different in lateral dimension as determined by TEM and AFM, while no significant differences were found in other properties. The second step was to characterize their possible cytotoxic effect and the impact of GO-S and GO-L on immune cell populations. We did not find significant differences in human PBMC viability by the exposure to both GO types. Such findings were in agreement with previous studies on macrophages.[18,37] Only few studies have been performed to date to understand the effect of graphene on the immune system,[12] and in addition most previous work focused only on the impact from graphene oxide exposure on traditional immunity markers, such as surface cluster of differentiation and cytokine release.[15,38] The understanding of how the immune system is regulated and responds to nanomaterials cannot overlook the genomic level.[22,39] Chatterjee et al. used an omics strategy to characterize the GO impact on hepatocytes (HepG2 cell line). They found a strong cytotoxic response induced by reduced GO mediated by a strong activation of Reacting Oxygen Species (ROS) pathways.[24] Following these considerations, we used here for the first time an omics approach to point out the global function of exposure of small-sized sheets of GO (GO-S) on immune cells using bead array

Illumina technology. In this study we found a well-detectable difference in immune gene expression profiling between the two GO types. Our results suggest that the different sizes of GO flakes can impact PBMCs at the molecular level. This finding was also in agreement with Russier et al.[18] who focused only on macrophages to demonstrate that the small size of GO can have a higher impact compared to the large size GO. Based on this data, the authors have proposed "the mask effect of graphene" suggesting that the small size GO has the capacity for higher interactions with the cell membrane, a greater ability to enter into the cells and, therefore, inducing more biological effects compared to large-sized GO.[18] In our work the effect of GO-S particularly enhanced genes such as IL1, IL6, IL10, TNF, CD40, CD80, and CSF2 related to the innate response and also other genes such as TBX21, CD86, and CCL5 related with the adaptive immunity, not leading to apoptosis or necrosis. Moreover, the only five genes upregulated by GO-L were also responsible for an innate immune cell response. In the same way Zhi et al. showed that the incubation with GO induced a specific activation of the innate immune system with a secretion of primary proinflammatory cytokines such as IL6, TNF, and IL1$\beta$.[40] The data obtained in our study by immune array provided convincing evidence that the adaptive immune response is not directly but indirectly affected by GO-S, due to the major effect on antigen presenting cells in terms of activation. Indeed, genes implicated in direct T cell activation such as IL2 and IFN$\gamma$ were not influenced. This was correlated with the absence of CD69 and CD25 expression, which is related to the IL2 secretion. To confirm the indirect activation of T cells we showed a clear enhancement of CD80 and TBX21, essential genes for efficient cell-mediated recruitment of T cells.[41] These observations were further supported by whole genome array data that identified the immune activation of some relevant pathways correlated with T cell chemotaxis: T cell migration, regulation of T cell chemotaxis, and leukocyte chemotaxis pathways. Intriguingly, we found in both T cell and monocytes the modulation of CXCL10 and related genes such as CXCR3, commonly activated during acute inflammatory processes.[42] The main mechanism of action of immunotherapeutic agents (i.e., anti-CTLA4 mAbs) is represented by the induction of specific chemokines (such as CXCL10 and CXCR3). These chemokines, by binding to their corresponding receptors, activated T helper 1 cells and NK cells which can mediate tumor rejection.[43]

We previously showed that functionalized CNTs could act only as "monocyte activating tools,"[22] while here we found that GO-S could impact on both T cell and monocyte gene expression. Indeed a direct impact of GO-S on T cells was found, with 1148 genes differentially expressed (738 genes upregulated, FC > 1) (Table S2, Supporting Information). We evidenced also the impact on TLR expression. Chen et al. found a GO-mediated TLR9 modulation inducing the expression of TNF receptor-associated factor 6 (TRAF6) that we have seen modulated also in our study, thus suggesting a similar induction mechanism.[44] However, further experiments are needed to assess a possible toll-like receptor mediated interaction, i.e., with specific siRNAs. Moreover, the GO-S mediated secretion of IL1$\beta$ and TNF cytokines is closely related to lymphocyte recruitment factors promoting the TLR mediated NF-kB and Mitogen-Activated Protein Kinase (MAPK) pathway activation and is associated with the TRAF family. Speculatively, we consider that GO-S could elicit an innate but also an adaptive response providing strong recruitment of immune cells (in tumors, for example), offering alternative strategies toward nanoimmunotherapeutics as suggested by Goldberg for other nanomaterials.[13] Another interesting effect of GO-S was on cell metabolism with a strong modulation of energetic pathways by a downregulation of OX-PHOs and mitochondrial ATP synthesis (Figure S6, Supporting Information) followed by a switch on of glycolytic pathways in both cell types. Normally the metabolic switch occurs in cancer cells that change their metabolic phenotypes to adapt to microenvironmental modifications giving a selective advantage to cancer cells under an unfavorable environment.[45] Fantin et al.[46] confirmed the metabolic switch of cancer cells by a glycolysis suppression, through the use of inhibitors such as lactate dehydrogenase A (LDH-A). The authors found significant inhibition of tumor proliferation when glycolysis was suppressed. Intriguingly, our data indicated that GO-S was able to strongly downregulate the oxidative phosphorylation pathways in the cell lines tested. This result is in agreement with the proteomic results of Zhou et al.[47] that showed a GO-induced inhibition of breast cancer cell metastases by selective downregulation of the protein Peroxisome Proliferator-Activated Receptor Gamma Coactivator 1 alpha (PGC-1$\alpha$), which accounts for the inhibition of OX-PHOs. Following these findings, a future perspective is the development of a nanosystem able to combine the action of our GO-S against the activation of oxidative phosphorylation pathway, with a targeted suppression of glycolysis through inhibitors such as LDH-A, may be effective in blocking cancer cell proliferation.

## 4. Conclusion

This work presented a wide-range approach to analyze the immunotoxicological impact of differently sized GOs on human PBMCs from healthy donors. We demonstrated that different dimensions of 2D graphene materials could regulate the immune response and the biological responses of immune cells reflected in the differential immune gene and activation molecular expression patterns. We found that thin (1-2 layer) GO sheets with small (<1 μm) lateral dimensions had a more pronounced effect on immune cells. Moreover, the whole genome expression assay data obtained from cells in response to small GO sheet interactions suggested many interesting pathways implicated that could in the future allow the exploration of novel graphene-based immunotherapeutic tools.

## 5. Experimental Section

*Synthesis and Characterization of Graphene Oxide*: GO was prepared by the modified Hummers' method in Ali-Boucetta et al.[7] with slight modifications. Briefly 0.2 g of graphite flakes (Barnwell, UK) was mixed with 0.1 g of $NaNO_3$ (Sigma-Aldrich, UK) and 4.6 mL of 96% $H_2SO_4$ (Fisher Scientific, UK). After obtaining a homogenous mixture, 0.6 g $KMnO_4$ (Sigma-Aldrich, UK) was then slowly added. Temperature was carefully monitored during the reaction and was kept between 98 and 100 °C. The mixture was further diluted with 25 mL of deionized $H_2O$ and 3% $H_2O_2$ (Sigma-Aldrich, UK) was added gradually for the reduction

of the residual $KMnO_4$, $MnO_2$, and $Mn_2O_7$. The resulting graphitic oxide suspension was exfoliated and purified by several centrifugation steps until the pH of the supernatant was ≈7 and a viscous orange/brown layer of pure GO appeared on top of the oxidation by-products and thick graphitic pieces. This layer was separated carefully and diluted in deionized water. TEM was performed using a BioTwin electron microscope (Philips/FEI), Tecnai 12 instrument operated at 120 kV accelerating voltage. A drop of sample was placed on a formvar/carbon coated copper grid. Excess material was removed by filter paper. Lateral size distributions were carried out using ImageJ software, after counting the lateral dimension of more than 100 individual GO sheets, from several TEM images. A multimode AFM was used on the tapping mode with an E-type scanner, Nanoscope VI controller, Nanoscope v614r1 control software (Veeco, Cambridge, UK) and a silicon tapping tip (NSG01, NTI-Europe, Apeldoorn, the Netherlands) of 10 nm curvature radius, mounted on a tapping mode silicon cantilever with a typical resonance frequency 150 kHz and a force 14 constant of 5.5 N $m^{-1}$. Images were captured in air, by depositing 20 µL of the GO dispersion on a freshly cleaved mica surface (Agar Scientific, Essex, UK) and allowed to adsorb for 30 s. Excess unbound material was removed by washing with filtered distilled water and then allowed to dry in air. Thickness distributions were carried out using ImageJ software, after counting the height of ≈100 individual GO sheets, from several AFM images. FT-IR was carried out on dry samples using a PerkinElmer Spectrum 100 spectrophotometer and the transmittance results were analyzed with the built-in spectrum software. For thermogravimetric analysis, we used a Pyris 6; Perkin-Elmer Ltd was used from 25 to 800 °C at 10 °C $min^{-1}$. Samples (1–2 mg) were weighed into a ceramic crucible. Nitrogen (20 mL $min^{-1}$) was used as a purge gas. Electrophoretic mobility ($\mu$) was measured by Malvern Zetasizer Nano ZS (UK) after dilution of samples with water in disposable Zetasizer cuvettes (Malvern Instruments). Default instrument settings and automatic analysis were used for measurements, $\mu$ was converted automatically by the equipment software to zeta potential ($\zeta$) values which is directly related to zeta potential by Henry's equation.[48] All values for samples prepared are triplicate measurements, values were mean ± SD. For Raman spectroscopy, all samples were recorded after preparing the aqueous dispersions and drop casting them on glass slides and evaporating the solvent. Measurements were carried out using a 50× objective at 633 nm laser excitation using a Renishaw micro-Raman spectrometer. An average of at least three different locations within each sample was measured. Absorbance spectroscopy of samples was measured by a Varian Cary winUV 50 Bio-spectrophotometer, USA. Samples were diluted 100 times in water before measurement in a 1 mL glass cuvette with 1 cm path length. Dual beam mode and baseline correction were used throughout the measurements to scan the peak wavelength and maximum absorbance between 200 and 800 nm.

*Cell Culture, Viability, and Activation*: Jurkat cells (T cell line), THP1 (monocyte cell line), and PBMCs were cultured as previously reported.[22] PBMCs were obtained from Ethylenediaminetetraacetic acid (EDTA)-venous blood samples from informed healthy male donors (25–50 years old) using a standard Ficoll-Paque (GE Healtcare) separation. Informed signed consent was obtained from all the donors. The cytotoxicity was evaluated by flow cytometry (FACS Canto, BD Biosciences, Mountain View, CA, USA). PBMCs were incubated for 24 h with increasing doses of GO-S and GO-L (25, 50, and 75 µg $mL^{-1}$). Ethanol was used as a positive control, while samples incubated with cell medium alone was used as negative control. All staining kits were purchased from Invitrogen, CA, USA: Annexin-V FITC (apoptosis), LIVE/DEAD FITC (late apoptosis and necrosis), and propidium iodide (necrosis). PBMCs were treated with GO at the intermediate concentration of 50 µg $mL^{-1}$ and stained to identify immune cell populations and activation markers, CD25 and CD69 (APC-conjugated anti-CD25, 2A3 clone, PE-conjugated anti-CD69, L78 clone, BD-Bioscience Mountain View, CA, USA). Concanavalin A (ConA, 4 µg $mL^{-1}$) and lipopolysaccharides (2 µg $mL^{-1}$) were used as positive controls (Sigma-Aldrich, St. Louis, Missouri, USA). Staining with fluorochrome-conjugated monoclonal antibodies was performed in the dark for 20 min. Cells were analyzed by flow cytometry.

*Immune Gene Array, Cytokine Assay, Microarrays*: Total RNA was extracted and RNA purification was performed with TriZol Reagent (TriZol, Invitrogen, Carlsbad, CA, USA). After extraction, cDNA synthesis was performed using a SuperScript III reverse transcriptase (Invitrogen, Carlsbad, CA, USA). The expression of 84 immune response genes were performed with a RT2 Profiler Polymerase Chain Reaction (PCR) Array (PAHS-052ZD, Superarray Bioscience Corporation, Frederick, MD) (instrument CFX96 Bio-Rad). Cell culture supernatants from PBMCs were used to quantify the secretion of cytokines using a MILLIPLEX MAP 10-plex Cytokine Kit (HCYTOMAG-60K -10, Millipore, Billerica, MA) (IL1$\alpha$, IL1$\beta$, IL2, TNF$\alpha$, IFN$\gamma$, IL6, IL8, IL10, IL4, CCL5). Experiments and statistical analysis were performed as previously showed.[22] Total RNA was extracted and purified using the RNAeasy mini kit (Qiagen, Valencia, CA, USA). RNA purity was assessed by spectrophotometric analysis and integrity by microfluidic molecular sizing using the Bioanalyzer 2100 (Agilent). Samples with RNA Integrity Number (RIN) less than eight were discarded. RNA (1 µg) was converted in cRNA and labeled (Illumina totalPrep RNA amplification kit, Ambion). Biotinylated cRNA was hybridized onto the Illumina HumanHT-12 v4 (Illumina, Inc., San Diego, CA, USA). The Illumina HumanHT-12 v4 interrogates the expression of 47.000 gene probes derived from the National Center for Biotechnology Information Reference Sequence RefSeq Release 38 (November 7, 2009) and other sources. Probe intensity and gene expression data were generated using the Illumina GenomeStudio software V2011.1 (Gene Expression Module V1.9.0).

*Statistical Analysis*: Statistical analyses for Raman $I_D/I_G$ and D band width were performed using Student's *t*-test (two-side *p*-value < 0.05). Data for Raman analysis and zeta potential are presented as mean ± SD. Data analysis for flow cytometry was performed using FACSDiva software (BD-Bioscience Mountain View, CA, USA). All the experiments were performed at least in triplicate. Statistical analyses for multiple cytokine assays were performed using Student's *t*-test. Data indicated with a star were considered statistically significant (two-side *p*-value < 0.05). Data are presented as mean ± SD. Multiplex ELISA tests on isolated human primary PMBCs were performed in samples from at least three different donors. Immune gene array data were analyzed by the comparative threshold cycle method. Relative quantification of gene expression using the $2 - \Delta\Delta Ct$ method correlated with the absolute gene quantification obtained using a standard curve. Data were analyzed with RT2 profiler PCR array data analysis software (http://pcrdataanalysis.sabiosciences.com/pcr/arrayanalysis.php). Whole genome expression measurements were extracted and normalized using the Illumina GenomeStudio software V2011.1 (Gene Expression Module V1.9.0). The same software was used for Quality Control (QC) analysis of the Beadchips. Statistical analysis and visualization of gene expression data were performed using BRB-ArrayTools, developed by R. Simon and the BRB-ArrayTools Development Team (http://linus.nci.nih.gov/BRB-ArrayTools.html). We identified genes that were differentially expressed among the two classes by using a multivariate permutation test.[49] We used the multivariate permutation test to provide 80% confidence that the proportion of false discoveries did not exceed 5%. The test statistics used are random variance *t*-statistics for each gene.[51] Although *t*-statistics were used, the multivariate permutation test is nonparametric and does not require the assumption of Gaussian distributions.

Genes whose expression was differentially regulated among the classes were clustered using Gene Ontology (gene on.). This analysis is different than annotating a gene list using gene on. categories. For each gene on. group, we computed the number *n* of genes represented on the microarray in that group, and the statistical significance *P*-value for each gene in the group. These *P*-values reflect differential expression among classes and were computed based on random variance *t*-tests or *F*-tests. For a gene on. group, two statistics are computed that summarize the *p*-values for genes in the group: the Fisher (LS) statistic and the Kolmogorov–Smirnov (KS) statistic as described in Simon R and Lam A. (Biometric Research Branch) BRB-ArrayTools User Guide, version 3.2. BRB, National Cancer Institute (http://linus.nci.nih.gov/brb). Samples of *n* genes are randomly selected from genes represented on the array and the summary statistic computed for those random samples. The

significance level associated with the gene on. category is the proportion of the random samples giving as large a value of the summary statistic as in the actual *n* genes of the gene on. category. For each gene on. category, two significance levels were computed corresponding to the two summary statistics. We considered a gene on. category significantly differentially regulated if either significance level was less than 0.01. We considered all gene on. categories between 5 and 100 genes represented on the array. Some of the categories were overlapping. We also uploaded the gene expression data to the "ingenuity pathway analysis" (ipa) to visualize the expression levels of genes in relevant pathway charts.

## Supporting Information

Supporting Information is available from the Wiley Online Library or from the author.

## Acknowledgements

This work was partly supported by the Fondazione Banco di Sardegna (Grant Nos. 2013.1308 and 2014.6035 to L.G.D.), the Sardinia Region (Grant No. CRP-59720 to L.G.D.), and the Gianfranco del Prete Association "The future: medicine, biology and nanotechnology Award" to L.G.D. L.G.D. acknowledge the Sardinian Region for supporting an Invited Professorship to A.B. The authors gratefully acknowledge financial support from EU FP7-ICT-2013-FET-F GRAPHENE Flagship project (Grant No. 604391). Authors declare that no conflict of interest exists.

Received: August 1, 2015
Revised: September 4, 2015
Published online: December 20, 2015

[1] A. K. Geim, K. S. Novoselov, *Nat. Mater.* **2007**, *6*, 183.
[2] G. Sechi, D. Bedognetti, F. Sgarrella, L. Van Eperen, F. M. Marincola, A. Bianco, L. G. Delogu, *Nanomedicine* **2014**, *9*, 1475.
[3] a) D. Bitounis, H. Ali-Boucetta, B. H. Hong, D. H. Min, K. Kostarelos, *Adv. Mater.* **2013**, *25*, 2258; b) M. Orecchioni, A. Bianco, L. G. Delogu, *Theranostics* **2015**, *5*, 710; c) P. Huang, C. Xu, J. Lin, C. Wang, X. Wang, C. Zhang, X. Zhou, S. Guo, D. Cui, *Theranostics* **2011**, *1*, 240.
[4] K. Kostarelos, K. S. Novoselov, *Science* **2014**, *344*, 261.
[5] S. Park, R. S. Ruoff, *Nat. Nanotechnol.* **2009**, *4*, 217.
[6] H. Ali-Boucetta, D. Bitounis, R. Raveendran-Nair, A. Servant, J. Van den Bossche, K. Kostarelos, *Adv. Healthc. Mater.* **2013**, *2*, 433.
[7] a) A. Bianco, *Angew. Chem.* **2013**, *52*, 4986; b) P. Wick, A. E. Louw-Gaume, M. Kucki, H. F. Krug, K. Kostarelos, B. Fadeel, K. A. Dawson, A. Salvati, E. Vazquez, L. Ballerini, M. Tretiach, F. Benfenati, E. Flahaut, L. Gauthier, M. Prato, A. Bianco, *Angew. Chem.* **2014**, *53*, 7714.
[8] a) C. Bussy, D. Jasim, N. Lozano, D. Terry, K. Kostarelos, *Nanoscale* **2015**, *7*, 6432; b) D. A. Jasim, C. Ménard-Moyon, D. Bégin, A. Bianco, K. Kostarelos, *Chem. Sci.* **2015**, *6*, 3952; c) B. Li, X. Y. Zhang, J. Z. Yang, Y. J. Zhang, W. X. Li, C. H. Fan, Q. Huang, *Int. J. Nanomed.* **2014**, *9*, 4697; d) M. Nurunnabi, Z. Khatun, K. M. Huh, S. Y. Park, D. Y. Lee, K. J. Cho, Y. K. Lee, *ACS Nano* **2013**, *7*, 6858.
[9] K. Wang, H. Song, J. Zhang, Y. Wo, S. Guo, D. Cui, *Nanoscale Res. Lett.* **2011**, *6*, 8.
[10] X. Wang, R. Podila, J. H. Shannahan, A. M. Rao, J. M. Brown, *Int. J. Nanomed.* **2013**, *8*, 1733.
[11] S. A. Sydlik, S. Jhunjhunwala, M. J. Webber, D. G. Anderson, R. Langer, *ACS Nano* **2015**, *9*, 3866.
[12] M. Orecchioni, D. Bedognetti, F. Sgarrella, F. M. Marincola, A. Bianco, L. G. Delogu, *J. Transl. Med.* **2014**, *12*, 138.
[13] M. S. Goldberg, *Cell* **2015**, *161*, 201.
[14] a) M. Lv, Y. Zhang, L. Liang, M. Wei, W. Hu, X. Li, Q. Huang, *Nanoscale* **2012**, *4*, 3861; b) M. Wojtoniszak, X. Chen, R. J. Kalenczuk, A. Wajda, J. Lapczuk, M. Kurzewski, M. Drozdzik, P. K. Chu, E. Borowiak-Palen, *Colloids Surf., B* **2012**, *89*, 79; c) S. Shi, K. Yang, H. Hong, H. F. Valdovinos, T. R. Nayak, Y. Zhang, C. P. Theuer, T. E. Barnhart, Z. Liu, W. Cai, *Biomaterials* **2013**, *34*, 3002.
[15] H. Yue, W. Wei, Z. Yue, B. Wang, N. Luo, Y. Gao, D. Ma, G. Ma, Z. Su, *Biomaterials* **2012**, *33*, 4013.
[16] A. Sasidharan, L. S. Panchakarla, P. Chandran, D. Menon, S. Nair, C. N. Rao, M. Koyakutty, *Nanoscale* **2011**, *3*, 2461.
[17] a) N. V. Vallabani, S. Mittal, R. K. Shukla, A. K. Pandey, S. R. Dhakate, R. Pasricha, A. Dhawan, *J. Biomed. Nanotechnol.* **2011**, *7*, 106; b) S. M. Kang, T. H. Kim, J. W. Choi, *J. Nanosci. Nanotechnol.* **2012**, *12*, 5185; c) W. Hu, C. Peng, W. Luo, M. Lv, X. Li, D. Li, Q. Huang, C. Fan, *ACS Nano* **2010**, *4*, 4317.
[18] J. Russier, E. Treossi, A. Scarsi, F. Perrozzi, H. Dumortier, L. Ottaviano, M. Meneghetti, V. Palermo, A. Bianco, *Nanoscale* **2013**, *5*, 11234.
[19] A. Sasidharan, L. S. Panchakarla, A. R. Sadanandan, A. Ashokan, P. Chandran, C. M. Girish, D. Menon, S. V. Nair, C. N. Rao, M. Koyakutty, *Small* **2012**, *8*, 1251.
[20] L. G. Delogu, E. Venturelli, R. Manetti, G. A. Pinna, C. Carru, R. Madeddu, L. Murgia, F. Sgarrella, H. Dumortier, A. Bianco, *Nanomedicine* **2012**, *7*, 231.
[21] C. Crescio, M. Orecchioni, C. Menard-Moyon, F. Sgarrella, P. Pippia, R. Manetti, A. Bianco, L. G. Delogu, *Nanoscale* **2014**, *6*, 9599.
[22] M. Pescatori, D. Bedognetti, E. Venturelli, C. Menard-Moyon, C. Bernardini, E. Muresu, A. Piana, G. Maida, R. Manetti, F. Sgarrella, A. Bianco, L. G. Delogu, *Biomaterials* **2013**, *34*, 4395.
[23] E. Frohlich, C. Meindl, K. Wagner, G. Leitinger, E. Roblegg, *Toxicol. Appl. Pharmacol.* **2014**, *280*, 272.
[24] N. Chatterjee, H. J. Eom, J. Choi, *Biomaterials* **2014**, *35*, 1109.
[25] H. H. Willard, L. L. MerrittJr., J. A. Dean, *Instrumental Methods of Analysis*, Wadsworth, Inc, Belmont, CA **1988**.
[26] G. X. Wang, B. Wang, J. Park, J. Yang, X. P. Shen, J. Yao, *Carbon* **2009**, *47*, 68.
[27] G. M. Neelgund, A. Oki, Z. Luo, *J. Colloid Interface Sci.* **2014**, *430*, 257.
[28] A. C. Ferrari, *Solid State Commun.* **2007**, *143*, 47.
[29] A. C. Ferrari, J. C. Meyer, V. Scardaci, C. Casiraghi, M. Lazzeri, F. Mauri, S. Piscanec, D. Jiang, K. S. Novoselov, S. Roth, A. K. Geim, *Phys. Rev. Lett.* **2006**, *97*, 187401.
[30] S. C. Rattana, N. Witit-anun, N. Nuntawong, P. Chindaudom, S. Oaew, C. Kedkeaw, P. Limsuwan, *Proc. Eng.* **2012**, *32*, 759.
[31] a) K. V. Krishna, C. Menard-Moyon, S. Verma, A. Bianco, *Nanomedicine* **2013**, *8*, 1669; b) X. Zhou, F. Liang, *Curr. Med. Chem.* **2014**, *21*, 855.
[32] a) V. Rastogi, P. Yadav, S. S. Bhattacharya, A. K. Mishra, N. Verma, A. Verma, J. K. Pandit, *J. Drug Deliv.* **2014**, *2014*, 670815; b) L. G. Delogu, A. Magrini, A. Bergamaschi, N. Rosato, M. I. Dawson, N. Bottini, M. Bottini, *Bioconj. Chem.* **2009**, *20*, 427; c) L. G. Delogu, S. M. Stanford, E. Santelli, A. Magrini, A. Bergamaschi, K. Motamedchaboki, N. Rosato, T. Mustelin, N. Bottini, M. Bottini, *J. Nanosci. Nanotechnol.* **2010**, *10*, 5293.
[33] L. Feng, Z. Liu, *Nanomedicine* **2011**, *6*, 317.
[34] a) L. G. Delogu, G. Vidili, E. Venturelli, C. Menard-Moyon, M. A. Zoroddu, G. Pilo, P. Nicolussi, C. Ligios, D. Bedognetti, F. Sgarrella, R. Manetti, A. Bianco, *Proc. Natl. Acad. Sci. USA* **2012**, *109*, 16612.

[35] M. A. Dobrovolskaia, S. E. McNeil, *Nat. Nanotechnol.* **2007**, *2*, 469.
[36] a) H. Zhou, K. Zhao, W. Li, N. Yang, Y. Liu, C. Chen, T. Wei, *Biomaterials* **2012**, *33*, 6933; b) A. V. Tkach, N. Yanamala, S. Stanley, M. R. Shurin, G. V. Shurin, E. R. Kisin, A. R. Murray, S. Pareso, T. Khaliullin, G. P. Kotchey, V. Castranova, S. Mathur, B. Fadeel, A. Star, V. E. Kagan, A. A. Shvedova, *Small* **2013**, *9*, 1686.
[37] a) G. Qu, S. Liu, S. Zhang, L. Wang, X. Wang, B. Sun, N. Yin, X. Gao, T. Xia, J. J. Chen, G. B. Jiang, *ACS Nano* **2013**, *7*, 5732; b) R. Feng, Y. Yu, C. Shen, Y. Jiao, C. Zhou, *J. Biomed. Mater. Res., Part A* **2014**, 103, 2006.
[38] Y. Li, Y. Liu, Y. Fu, T. Wei, L. Le Guyader, G. Gao, R. S. Liu, Y. Z. Chang, C. Chen, *Biomaterials* **2012**, *33*, 402.
[39] P. Ricciardi-Castagnoli, F. Granucci, *Nat. Rev. Immunol.* **2002**, *2*, 881.
[40] X. Zhi, H. Fang, C. Bao, G. Shen, J. Zhang, K. Wang, S. Guo, T. Wan, D. Cui, *Biomaterials* **2013**, *34*, 5254.
[41] a) K. N. Nielsen, M. A. Steffensen, J. P. Christensen, A. R. Thomsen, *J. Immunol.* **2014**, *193*, 1223; b) D. Zhang, X. Zhang, M. Ge, M. Xuan, H. Li, Y. Yang, R. Fu, F. Zhou, Y. Zheng, R. Yang, *Hum. Immunol.* **2014**, *75*, 129.
[42] L. M. Coussens, Z. Werb, *Nature* **2002**, *420*, 860.
[43] D. Bedognetti, E. Wang, M. R. Sertoli, F. M. Marincola, *Expert Rev. Vaccines* **2010**, *9*, 555.
[44] G. Y. Chen, C. L. Chen, H. Y. Tuan, P. X. Yuan, K. C. Li, H. J. Yang, Y. C. Hu, *Adv. Healthcare Mater.* **2014**, *3*, 1486.
[45] J. Zheng, *Oncol. Lett.* **2012**, *4*, 1151.
[46] V. R. Fantin, J. St-Pierre, P. Leder, *Cancer Cell* **2006**, *9*, 425.
[47] T. Zhou, B. Zhang, P. Wei, Y. Du, H. Zhou, M. Yu, L. Yan, W. Zhang, G. Nie, C. Chen, Y. Tu, T. Wei, *Biomaterials* **2014**, *35*, 9833.
[48] A. Adamson, *Physical Chemistry of Surfaces*, Wiley Interscience, New York **1990**.
[49] R. M. Simon, E. Korn, L. McShane, M. Radmacher, G. Wright, Y. Zhao, *Desing and Analysis of DNA Microarray investigations*, Springer-Verlag, New York **2003**.
[50] G. W. Wright, R. M. Simon, *Bioinformatics* **2003**, *19*, 2448.